

Synthesis of Binder-Free, Low-Resistant Randomly Orientated Nanorod/Sheet ZnS–MoS₂ as Electrode Materials for Portable Energy Storage Applications

Asif Raza, Abdur Rasheed, Amjad Farid, Misbah Yousaf, Noman Ayub, and Ijaz Ahmad Khan*



Cite This: *ACS Omega* 2024, 9, 27919–27931

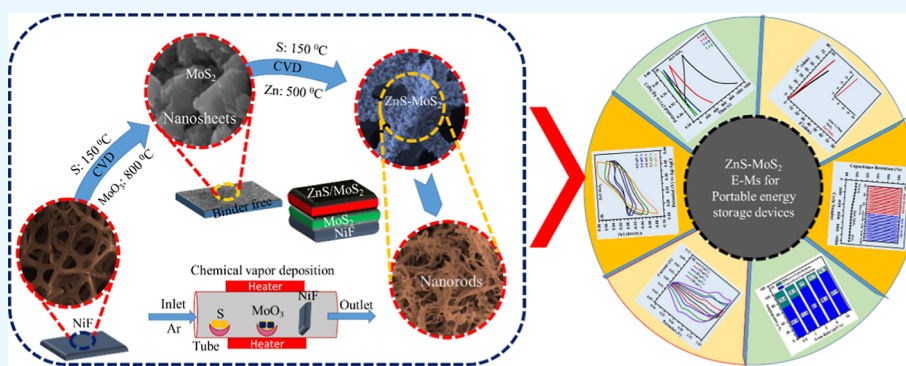


Read Online

ACCESS |

Metrics & More

Article Recommendations



ABSTRACT: The scientific community needs to conduct research on novel electrodes for portable energy storage (PES) devices like supercapacitors (S–Cs) and lithium-ion batteries (Li-ion-Bs) to overcome energy crises, especially in rural areas where no electrical poles are available. Herein, the nanostructured MoS₂ and ZnS–MoS₂ E-Ms consisting of nanoparticles/rods/sheets (N-Ps-Rs-Ss) are deposited on hierarchical nickel foam by a homemade chemical vapor deposition (H-M CVD) route. The X-ray diffraction patterns confirm the formation of polycrystalline films growing along various orientations, whereas the field-emission scanning electron microscope analysis confirms the formation of N-Ps-Rs-Ss. The change in structural and microstructural parameters indicates the existence of defects improving the energy storage ability of the deposited ZnS–MoS₂@Ni–F electrodes. The specific capacitances of MoS₂@Ni–F and ZnS–MoS₂@Ni–F electrodes are found to be 1763 and 3565 F/g at 0.5 mV/s and 1451 and 3032 F/g at 1 A/g, respectively. The growing behavior of impedance graphs indicates their capacitive nature; however, the shifting of impedance curves toward y -axis indicates that the increasing diffusion rates due to the formation of nanostructures of ZnS–MoS₂ results in low impedance. An excellent energy storage performance, minimum capacity fading, and improved electrical conductivity of the deposited E-Ms are due to the combined contributions of the electrical double layer and pseudocapacitor nature, which is again confirmed by theoretical Dunn's model. The absence of charge transfer resistance and good capacitance retention (95%) even after 10,000 cycles indicates that the deposited E-Ms are better for PES devices like S–Cs and Li-ion-Bs than MoS₂ E-Ms. The assembled asymmetric supercapacitor device exhibited the maximum specific capacitance = 996 F/g, energy density = 354–285 W h/kg, power density = 2400–24,000 W/kg, capacitance retention = 95% and Coulombic efficiency = 100% even after a long charging–discharging of 10,000 cycles.

1. INTRODUCTION

The growing technology has increased the utilization of conventional energy resources like fossil fuels to fulfill the energy demands. The utilization of conventional energy resources at a large scale is not only creating the energy crisis but is also responsible for changing the global climate as well as increasing environmental pollution.^{1,2} However, modern society can also face some unmanageable and unembellished difficulties if no attention is paid to the energy crisis. Currently, the production of energy is smaller than the demand of modern society.³ Such energy crises motivate the researchers

to fabricate sustainable, environment-friendly, clean, and portable energy storage (PES) devices.⁴ Among them, lithium-ion batteries (Li-ion-Bs) and supercapacitors (S–Cs) are potential candidates to overcome the energy crisis of the

Received: November 30, 2023

Revised: March 23, 2024

Accepted: April 5, 2024

Published: June 24, 2024



Table 1. Detailed Deposition Parameters of MoS₂@Ni–F and ZnS–MoS₂@Ni–F

E-Ms	wt. of RMs (mg)		distance of RMs from Ni–F (cm)		temperature of RMs (°C)		AGFR and deposition time	
	S	MoO ₃	S	MoO ₃	S	MoO ₃	(sccm)	min
MoS ₂	80	30	35	17	150	800	350	5
ZnS–MoS ₂	S	Zn	S	Zn	S	Zn		
	30	30	30	15	150	500		

global world. The Li-ion-Bs and S–Cs are preferred due to the outstanding electrochemical properties like charging–discharging capacity, capacity fading, capacity retention (CR), Coulombic efficiency (CE), energy density (E_d), power density (P_d), specific capacitance (C_{cv} and C_{cd}), and excellent cyclic stability (C–S).^{5–8} The Li-ion-Bs and S–Cs are widely used in various fields including transport, military telecommunication systems, consumer electronics, and electrical vehicles.^{9–12} The above-mentioned PES devices can also be adopted to overcome the energy crises in rural areas in the absence of electricity supply.

Based on the electrochemical performance (ECP) of PES devices, the S–Cs are categorized into the electrical double layer capacitors (EDLCs) having a simulation of charges at the interface between electrolyte and surface of electrodes and the pseudocapacitors (P–Cs) exhibiting redox reactions.¹³ The performance of Li-ion-Bs and S–Cs is related to the deposition route, type, and surface morphological features of deposited electrodes used for their fabrication. Amid these electrodes, carbon and transition metal oxides/dichalcogenides (TMOs/TMDCs) like V₂O₅, MoO₃, ZnO, zinc sulfide (ZnS), CuS, NiS, and MoS₂ are investigated for use as electrodes for good ECP of PES devices.^{14–20} Amid TMDCs, MoS₂ is a noteworthy electrode for PES devices; however, its ECP can be tuned by modifying its structure and microstructures to increase the surface area that may accumulate more electrolytic ions, resulting in enhanced specific capacitance.^{21–23} The MoS₂ materials are mostly used in gas sensing and lubrication, and the ECP of the deposited electrodes can be improved by loading hydrogen.^{24–28} It is noticeable that the MoS₂ electrodes have larger conductivity and storage ability as compared to other TMOs as well as carbon and graphite-based nanostructured electrodes.^{29–31} The MoS₂ electrodes synthesized by simple physical vapor deposition route has a C_{cv} of 12.21 F/g at 10 mV/s.³² It has been pointed out that for the MoS₂ electrodes deposited via the hydrothermal route, C_{cd} = 249 F/g at 2 A/g.³³ Moreover, the MoS₂ electrodes deposited via the hydrothermal route has the C_{cv} value of 766 F/g at 1 mV/s.³⁴

Before the description of the deposition route, the concept of different electronegativities of components [including sulfur (S) and molybdenum (Mo)] for MoS₂ electrodes is very important. The negligible electronegativity of S and Mo atoms helps overcome volume expansion during charging–discharging measurements, stable defect-rich active sites, and maximum electron/ion interactions for improving ECP. The ECP of the MoS₂ electrode can be improved by modifying their physical properties, which can be changed by changing the deposition routes. Mostly, a time-consuming and costly hydrothermal route is adopted to deposit the MoS₂ electrode, showing weak ECP. In order to improve the ECP of electrodes, it is necessary to modify their physical properties by selecting the cost-effective homemade chemical vapor deposition (H-M CVD) route. The energy storage ability of the MoS₂ electrode is

smaller than current demands due to their layer's agglomeration, volume expansion, low specific capacitance, low charging–discharging rate, unsatisfactory cyclic life, and limited defect-rich active sites. Therefore, it is necessary to improve the ECP of the MoS₂ electrode by nanostructure formation with different metal sulfides. Amid these metal sulfides, ZnS is more appropriate to enhance the ECP of the MoS₂ electrodes. However, very limited information is available in the literature about the nanostructure formation of the MoS₂ electrode with ZnS and other metal sulfides.^{35,36} Such nanostructured electrodes are deposited by different routes such as hydrothermal,³⁷ chemical bath deposition,³⁸ liquid exfoliation,³⁹ and evaporation.⁴⁰ Therefore, the increment in energy storage ability of the nanostructured MoS₂ electrode is vital to increase the ECP of PES devices.

In the current research, the MoS₂ and nanostructured ZnS–MoS₂ electrodes are deposited on nickel foam (Ni–F) by the H-M CVD route. The vertically growing fiber-like nanosheets forming a cone-like columnar structure of the MoS₂@Ni–F electrode is changed into a complicated network of nanonoodles when the ZnS material is condensed on a MoS₂ electrode. However, the nanostructural analysis reveals that the surface microstructure of ZnS–MoS₂@Ni–F is more interesting (high porosity) as compared to a low porosity microstructure of MoS₂@Ni–F. The more porous nanostructure-based ZnS–MoS₂@Ni–F electrode exhibited an excellent ECP showing high values of C_{cv} of 3565 F/g, which is 2 times more than the C_{cv} of the MoS₂ electrode at 0.5 mV/s. The absence of a semicircle in the impedance spectrum is attributed to good electrical conductivity, resulting in high charge storage capability and hence excellent ECP. The deposited ZnS–MoS₂@Ni–F exhibited 95% CR and 100% CE for 10,000 cycles. Based on Dunn's model calculations, the capacitive controlled contributions (66–90%) of the ZnS–MoS₂@Ni–F electrode is more than diffusion-controlled contributions (34–10%) at 0.5, 1, 3, 5, and 10 mV s^{−1}. The higher ECP of the deposited ZnS–MoS₂@Ni–F electrode is due to the combined (capacitive and diffusion) controlled contributions (P–Cs and EDLC behavior). The assembled asymmetric S–Cs device exhibited a C_{cd} of 996 F/g at 3 A/g. The excellent ECP of ZnS–MoS₂@Ni–F is associated with the development of (i) nanostructured MoS₂ and ZnS layers, (ii) complicated porous network of nanonoodles, (iii) high surface area, (iv) excellent synergistic effects between active species and substrate, and (v) combined controlled capacitive and diffusive contributions.

2. EXPERIMENTAL DETAILS

2.1. Electrode Material Deposition. The nanostructured MoS₂@Ni–F and ZnS–MoS₂@Ni–F are deposited by the H-M CVD route by using standard grade [Sigma-Aldrich] raw materials (RMs) like MoO₃, S, and Zn. Table 1 demonstrates the different weights (wt) of RMs employed to deposit MoS₂@Ni–F and ZnS–MoS₂@Ni–F electrodes. The wt. of RMs used to deposit these electrodes are measured by high

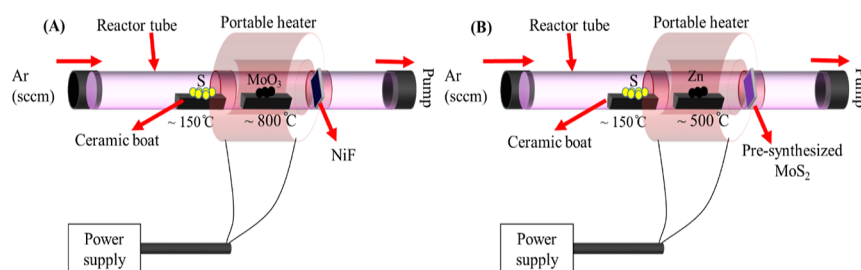


Figure 1. Schematic diagram of H-M-CVD employed to deposit (A) $\text{MoS}_2@Ni-F$ and (B) $\text{ZnS-MoS}_2@Ni-F$.

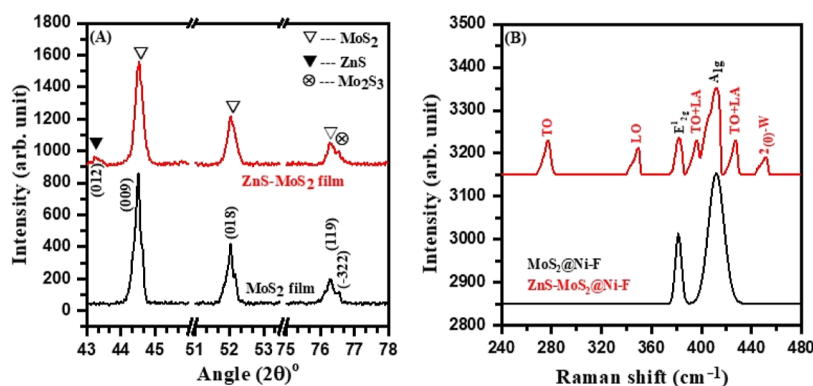


Figure 2. XRD (A) and Raman (B) analysis of $\text{MoS}_2@Ni-F$ and $\text{ZnS-MoS}_2@Ni-F$ electrodes.

precision weight balance (minimum reading = 0.001 g). The schematic diagram shows the mechanism employed to deposit MoS_2 and nanostructured $\text{ZnS-MoS}_2@Ni-F$ (Figure 1A,B), respectively. Basically, the H-M CVD route is assembled by a portable heater connected to a reactor tube (R-T), which is connected to the gas flow meter, gas cylinder, rotary vane pump, pressure measuring gauge, and temperature meter connected to the thermocouple. However, a further explanation of the H-M CVD route can be found in the literature.^{41–43} For the deposition of $\text{MoS}_2@Ni-F$, the MoO_3 , S, and Ni-F are placed on their appropriate positions within the R-T according to the parameters demonstrated in Table 1. After assembling the H-M CVD system, the rotary pump is switched on to develop vacuum (10^{-2} mbar) within the R-T. After achieving proper vacuum, the portable heater mounted on R-T is connected to a voltage regulator to provide energy to the RMs placed within the R-T. The energies of RMs are controlled by adjusting the voltage through a voltage controller. When MoO_3 and S species get sufficient amounts of energy, resulting in their bonds breaking, it results in evaporation. The evaporated species of MoO_3 and S are carried by the argon gas flow rate (AGFR) toward the Ni-F surface. According to our previous research data, the involved accelerated evaporated species may or may not react to each other depending on their ability to get energy and hence condense on the surface of Ni-F.

However, the increasing/decreasing temperature profile of the deposition process is given in the literature.⁴⁴ For the deposition of $\text{ZnS-MoS}_2@Ni-F$, the predeposited $\text{MoS}_2@Ni-F$ electrodes are treated in evaporated Zn and S plasma. The reaction kinetics for the deposition of $\text{MoS}_2@Ni-F$ and $\text{ZnS-MoS}_2@Ni-F$ is demonstrated, as the increasing applied voltage through the voltage regulator increases the energy of RMs placed in ceramic boats, resulting in bond-breaking, which evaporates the RMs. The evaporated species are accelerated by AGFR toward the surface of Ni-F, and during

their kinetic, the evaporated species can react with each other and condense on the surface of Ni-F.

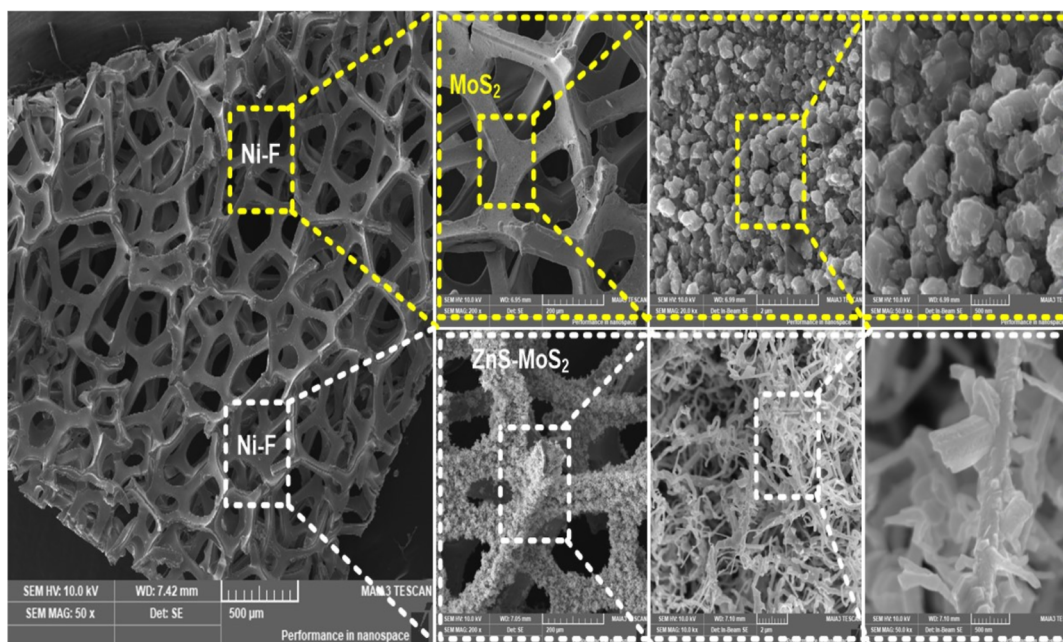
2.2. Material Characterizations. The different properties such as structure, microstructure, vibrational, composition, and electrochemical properties of the deposited nanostructured $\text{MoS}_2@Ni-F$ and $\text{ZnS-MoS}_2@Ni-F$ are investigated by X-ray diffraction (XRD) (“Model: D-8-ADVANCE; $\theta-\theta$ ” diffractometer, $\text{CuK}\alpha$ radiation, wavelength = 1.5406 Å”, Raman spectroscopy (RS) “MN STEX-PRI100 with wavelength = 633 nm”, field-emission scanning electron microscope “TESCAN-MIRA-3” attached with an energy-dispersive spectroscopy (EDX), and potentiostatic “CS350M”. The ECP parameters such as cyclic voltammetry (CV), galvanostatic charging/discharging (GCD), and electrochemical impedance spectroscopy (EIS) of working $\text{MoS}_2@Ni-F$ and $\text{ZnS-MoS}_2@Ni-F$ electrodes are evaluated by the reference (Ag/AgCl) and counter (platinum plate) electrodes in 2 M KOH electrolyte solution, respectively. Moreover, the charging–discharging capacity, capacity fading, CR, CE, E_d , P_d , C_{cv}/C_{cd} , and C–S of the deposited $\text{MoS}_2@Ni-F$ and $\text{ZnS-MoS}_2@Ni-F$ electrodes are calculated. The calculations of theoretical Dunn’s model are investigated to understand the experimental results of deposited electrodes.

3. RESULTS AND DISCUSSIONS

3.1. Structural Properties. The characterization techniques such as XRD and RS are performed to study the structure of the $\text{MoS}_2@Ni-F$ and $\text{ZnS-MoS}_2@Ni-F$ electrodes (Figure 2A,B). The XRD analysis of the nanostructured $\text{MoS}_2@Ni-F$ and $\text{ZnS-MoS}_2@Ni-F$ electrodes is shown in Figure 2A. The different diffraction planes including (009), (018), and (119) that appeared at $2\theta = 44.48$, 52.03, and 76.29 are attributed to individual MoS_2 phases having a rhombohedral crystal structure [ref. cards: 01-086-2308], while the plane (012) that appeared at 43.35° is attributed to the c-ZnS phase

Table 2. Calculated the Structure Parameters of the Deposited MoS₂@Ni–F and ZnS–MoS₂@Ni–F Electrodes

electrodes	phases	<i>h k l</i>	angle (2θ)°	intensity	fwhm (degree)	crystallite-size (nm)	dislocation density $\times 10^{-4}$ (nm) ⁻²	microstrains $\times 10^{-2}$
MoS ₂	MoS ₂	(009)	44.48	819.16	0.25	30.97	10.42	5.78
		(018)	52.03	368.98	0.29	27.50	13.21	6.51
		(119)	76.29	145.89	0.19	47.97	4.34	3.73
ZnS–MoS ₂	MoS ₂	(-322)	76.55	71.23	0.13	70.23	2.02	2.55
		(009)	44.50	634.16	0.28	27.66	13.07	6.47
		(018)	52.05	297.04	0.30	26.59	14.14	6.74
	MoS ₂	(119)	76.29	135.55	0.17	53.62	3.47	3.34
		(-322)	76.55	70.02	0.20	45.65	4.79	3.92
		ZnS	(012)	43.35	50.05	0.10	77.13	1.68

Figure 3. Microstructural analysis of bare Ni–F (Mag: 50X), MoS₂@Ni–F (Mag: 200X, 2kX, 50 KX), and ZnS–MoS₂@Ni–F (Mag: 200X, 2kX, 50 KX) electrodes.

of the ZnS–MoS₂@Ni–F electrode [ref. cards 00-012-0688]. The absence of a diffraction plane related to the MoO₃ compound indicates its complete decomposition into Mo and O species. The evaporated Mo species react with S to form MoS₂ and Mo₂S₃ phases; however, the O species could not react with metals due to smaller energy fluxes and escape from the R–T along with the carrier gas. The up-shifting of diffraction planes and development of structural defects like dislocation density, stresses, microstrains, and lattice distortion are produced due to solid solution formation by overlapping the different diffraction planes of ZnS and MoS₂ phase [ref. cards: 00-001-0677, 00-002-0564, 00-012-0688, 00-039-1363]. These structural deformations are responsible for forming nanostructured porous surface morphology that results in excellent ECP of S–Cs made by the deposited ZnS–MoS₂@Ni–F electrode. The formation of a nanostructured ZnS–MoS₂@Ni–F electrode may also be responsible for improving the ECP parameters (discussed later). The full width at half maxima (fwhm) of any diffraction plane is used to determine the crystallite size, whereas the dislocation density and microstrains of the nanostructured electrodes are determined by following formulas.^{41,45}

$$\text{Crystallite - size} = \frac{k\lambda}{\text{FWHM}(\cos \theta)} \quad (1)$$

$$\text{Dislocation - density} = \frac{1}{(\text{Crystallite - size})^2} \quad (2)$$

$$\text{microstrain} = \frac{\text{FWHM}(\cos \theta)}{4} \quad (3)$$

where K , λ , and θ are the numerical constant (0.89), wavelength of incident radiations (1.54 Å), and Bragg's angle, respectively. The development of different diffraction planes of MoS₂@Ni–F and ZnS–MoS₂@Ni–F electrodes indicates the formation of polycrystalline nanostructured electrodes.

When ZnS material is deposited on the already deposited MoS₂@Ni–F electrode, the peak intensity of different planes of the MoS₂ phase is reduced. The decreasing peak intensity confirmed the condensation of ZnS on the MoS₂ surface, resulting in nanostructured growth of ZnS–MoS₂@Ni–F electrodes. The increase in structure defects such as fwhm, dislocation density, and microstrains is responsible for decreasing the peak intensity, resulting in lattice distortion. The increment in the structure defects may be due to heterostructure formation between ZnS and MoS₂ materials. Table 2 also demonstrates the variations in different structure parameters of the MoS₂@Ni–F and ZnS–MoS₂@Ni–F electrodes. The variations in different structure parameters

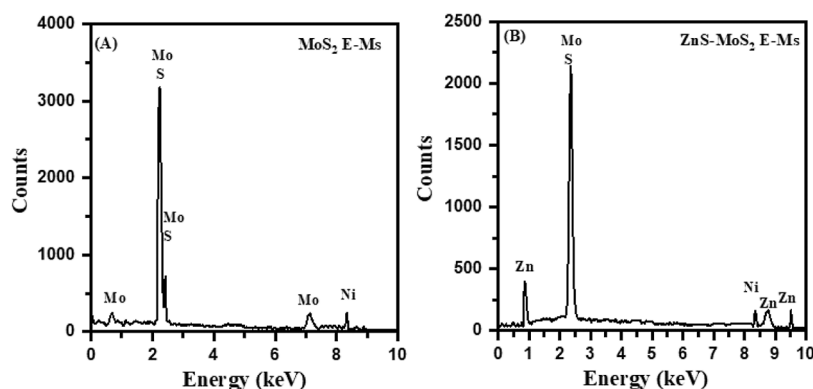


Figure 4. EDX spectra of the already-deposited (A) $\text{MoS}_2@Ni-F$ and (B) $\text{ZnS-MoS}_2@Ni-F$ electrodes.

are responsible for creating the above-mentioned structure defects, which are increased due to the nanostructure formation of $\text{ZnS-MoS}_2@Ni-F$ electrodes. Additionally, stress and microstrains are also produced due to up/down shifting of different diffraction planes of the $\text{MoS}_2@Ni-F$ electrode. The up-shifting shows the existence of compressive stress, while the shifting toward a lower angle shows the development of tensile stress.⁴² In our case, the shifting of the diffraction plane toward a higher angle shows the development of compressive stresses in the deposited electrodes shrinking the d -spacing, which is due to the formation of solid solution (already discussed) of ZnS and MoS_2 phases.^{46,47} It means that the presence of two phases in a solid solution can make bonds; however, they may be weak or strong depending on their available energy associated with the surface and strain energies. In our case, no clearly observed diffraction planes of ZnS-MoS_2 phase indicate the formation of weak bonds and just solid solution is formed (already discussed).

The Raman analysis is further carried out to examine the structural properties of $\text{MoS}_2@Ni-F$ and $\text{ZnS-MoS}_2@Ni-F$ electrodes. Figure 2B demonstrates the vibrational modes presented in the deposited $\text{MoS}_2@Ni-F$ and $\text{ZnS-MoS}_2@Ni-F$ electrodes. The $\text{MoS}_2@Ni-F$ electrodes present two vibrational (E_{2g}^1 and A_{1g}) modes located at 381 and 412 cm^{-1} .^{48–50} It is known that the ZnS phase shows 5 vibrational modes like optical (To), longitudinal (LO), and combined (To + LA), whose locations are close to the observed positions: ~ 275 , ~ 348 , ~ 397 , ~ 427 , and ~ 452 cm^{-1} .^{51–53} The vibrational A_{1g} mode is more intense, which indicates the defect-rich active sites along the c -direction. The intensity of MoS_2 vibrational modes is slightly decreased when ZnS material is condensed on the already deposited $\text{MoS}_2@Ni-F$ electrode; however, the diffusion of involved species such as Zn and S into the lattice of MoS_2 compound distorts its lattice. The heterostructure formation between ZnS and MoS_2 materials is responsible for creating defect-rich active sites due to the development of the above-mentioned defects.

3.2. FESEM Analysis. The microstructural features impressively incite the energy storage ability of the deposited $\text{MoS}_2@Ni-F$ and $\text{ZnS-MoS}_2@Ni-F$ electrodes. It is known that the energy storage ability is dependable on the surface morphology such as porosity, surface area, distribution and compactness of nanostructured electrodes. The FESEM analysis is performed to investigate the microstructural features of $\text{MoS}_2@Ni-F$ and $\text{ZnS-MoS}_2@Ni-F$ electrodes. Figure 3 shows the microstructural features of $Ni-F$, $\text{MoS}_2@Ni-F$, and $\text{ZnS-MoS}_2@Ni-F$ electrodes. The microstructure of bare

$Ni-F$ shows the formation of interconnected rods, indicating its better electronic conductivity. The wide vacant spaces in the microstructure are responsible for the larger diffusion of electrolyte ions. The surface microstructures of the deposited $\text{MoS}_2@Ni-F$ electrode are not obvious at a small magnification (200 μm), while it becomes noticeable at high magnification (2 μm and 500 nm). At high magnification, the microstructure comprises fiber-like nanosheets stacking one above the other, forming a columnar structure that looks like vertical growth. The sharp top edge of the columnar structure is similar to cones like shape. The height of columnar cones is different, which makes the surface rough, whereas the various distances between two columnar cones again show the formation of a rough surface. The overall nanostructural view is like the moving waves comprising crusts and troughs. The formation of a rough surface may be more suitable for the diffusion of ions performing an excellent intercalation process, enhancing the ECP of the deposited electrode.⁴⁸ The microstructural features of the $\text{MoS}_2@Ni-F$ electrode are totally changed by the condensation of the ZnS material on the MoS_2 surface. At low magnification, the microstructure of the $\text{ZnS-MoS}_2@Ni-F$ electrode is composed of vertically mounting glossy nanoparticles forming a complex distribution on the whole scanned surface. At higher magnification, the microstructure of $\text{ZnS-MoS}_2@Ni-F$ electrodes is the noodle-like complex network; however, the cross-linkage of the noodles forms a rough surface, which assists the ECP because it has been noted that the electrodes having noodle-like surface morphology show excellent ECP through the intercalation process. Deep investigation shows that the formation of long nanorods of diameter ~ 250 nm are observed. Some nanoparticles of undefined dimensions are attached to the long nanorods. The horizontally stacked nanosheets are also attached to the long nanorods as well as the noodles like network. Such a type of distribution of nanodimensional microstructures leads to a complicated but porous surface morphology. One part of the FESEM microstructure is more porous, while the other part contains nanonoodle-, nanorod-, and nanosheet-like features. The microstructure of the nanostructured $\text{ZnS-MoS}_2@Ni-F$ electrode is significantly porous as compared to the microstructure of the $\text{MoS}_2@Ni-F$ electrode. Additionally, the surface roughness and empty regions of the nanostructured $\text{ZnS-MoS}_2@Ni-F$ electrode are significantly larger than those of the $\text{MoS}_2@Ni-F$ electrode. The interconnection of noodles can also increase the diffusion and hence fast reaction kinetics of electrolytic ions for improving the ECP. The intertwined nanorods and stacking

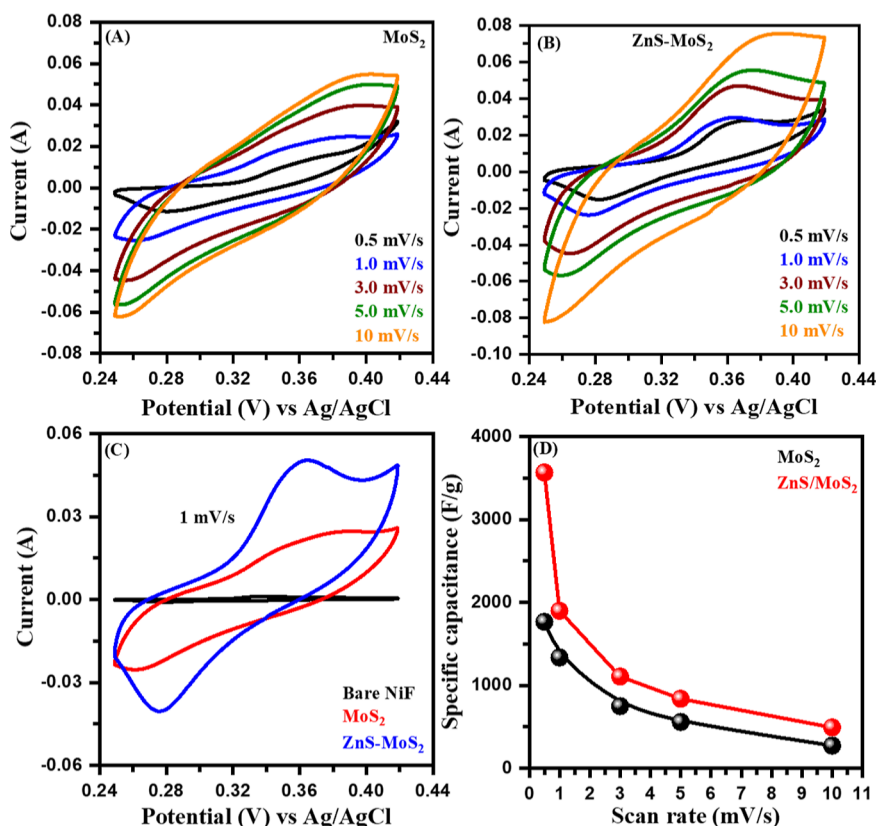


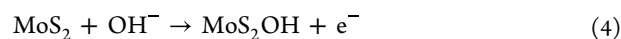
Figure 5. CV profiles of nanostructured MoS₂@Ni-F (A) and ZnS-MoS₂@Ni-F electrodes (B), combined CV profiles at 1 mV/s (C) and the calculated C_{cv} values (D) at various scan rates.

of horizontal nanosheets help overwhelm the volume enlargement during the charge/discharge mechanism.

It is concluded that the porous and rough nanostructural features comprising nanoparticles/rods/sheets (N-Ps-Rs-Ss) enable the deposited MoS₂@Ni-F and ZnS-MoS₂@Ni-F electrodes to present both P-Cs and EDLC characteristics. The observed microstructures are responsible for enlarging the surface area, porosity, and accessibility of huge electrolytic ions to the large surface area of the deposited electrodes and hence enhancing the ECP of the nanostructured ZnS-MoS₂@Ni-F electrode. The EDX measurements are studied to determine the wt % of various elements present in the deposited MoS₂@Ni-F and ZnS-MoS₂@Ni-F electrodes (Figure 4A,B). The EDX peaks associated with Ni, Mo, S, and Zn indicate the successful deposition of MoS₂@Ni-F and ZnS-MoS₂@Ni-F electrodes. The EDX peak associated with Ni comes from the Ni-F. The wt % of Mo and S for MoS₂ and Mo, Zn, and S in the ZnS-MoS₂@Ni-F electrode is found to be 27.3 and 24.2 and 27.5, 22.5, and 23.7, respectively. The absence of EDX peaks related to impurity confirmed the purity and successful deposition of nanostructured MoS₂@Ni-F and ZnS-MoS₂@Ni-F electrodes on the surface of Ni-F.

3.3. Electrochemical Performance. The ECP-like capacitive and charging/discharging rate of the deposited nanostructured MoS₂@Ni-F and ZnS-MoS₂@Ni-F electrodes is studied by CV, GCD, and EIS measurements. The electrochemical cell of a workstation comprising three electrodes is assembled in the presence of 2 M KOH electrolytic solution. The CV profiles of the nanostructured MoS₂@Ni-F and ZnS-MoS₂@Ni-F electrodes at 0.5, 1, 3, 5, and 10 mV/s with the voltage ranged from 0.25 to 0.42 V,

respectively (Figure 5A,B). The presence of redox peaks indicates that both the deposited electrodes show P-C behavior in KOH solution. The kinetic equation representing the redox reaction is given by



The current generation and redox peak broadening are increased, but the shape of CV profiles remains constant, indicating an excellent rate capability and scan stability of the deposited electrodes. The shifting of redox peaks toward higher/lower potential indicates that the deposited electrodes can be used as Li-ion-Bs. The CV curves become flat at higher scan rates, which means that at a lower scan rate, the deposited electrodes behave like P-Cs, while at higher scan rates, it behaves like EDLC.⁵⁴ The capacitive role is significant at higher scan rates because a restricted time is presented for the electrolytic ions to intercalate through the rough porous surface of electrodes. This hybrid CV profile of the deposited electrodes enables them to expedite the electrochemical stability at higher scan rates and is responsible for enhancing the material stability over increasing scan rates. The C_{cv} values of the deposited MoS₂@Ni-F and ZnS-MoS₂@Ni-F electrodes can be calculated from the CV profiles by the formula.⁵⁵

$$C_{cv} = \frac{\int I dv}{2 \times v \times \Delta V \times m} \quad (5)$$

where $\int I dv$ is the integral area of the CV profile, ΔV is the potential difference, v is the scan rate (mV/s), and m is the active mass of the deposited nanostructured MoS₂@Ni-F and ZnS-MoS₂@Ni-F electrodes. The measured C_{cv} values of the

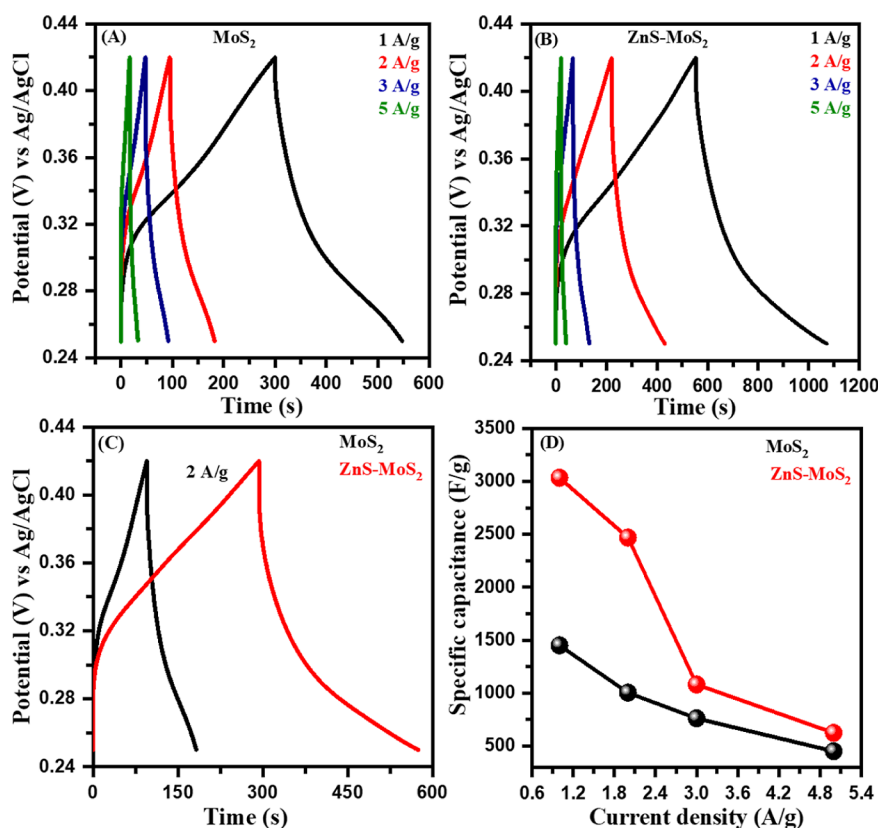


Figure 6. GCD profiles of the nanostructured MoS₂@Ni-F (A) and ZnS-MoS₂@Ni-F electrodes (B), the combined GCD profiles at 2 A/g (C), and the calculated C_{cd} values (D) at 1, 2, 3, and 5 A/g.

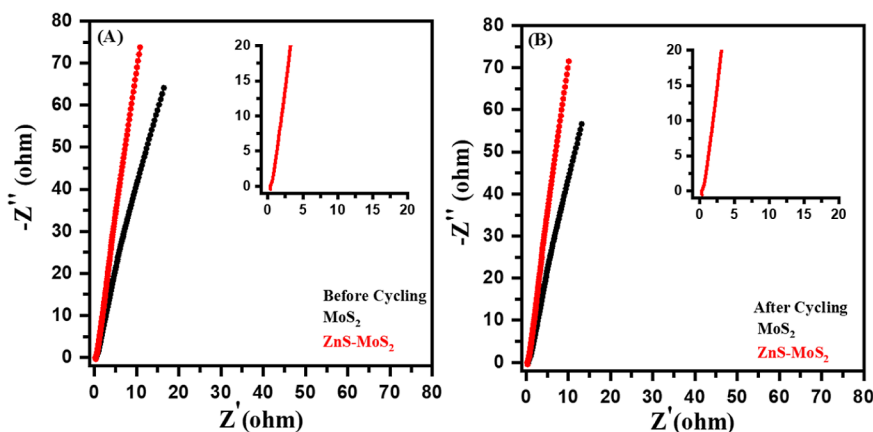


Figure 7. EIS profiles of the nanostructured MoS₂@Ni-F and ZnS-MoS₂@Ni-F electrodes before (A) and after (B) 10,000 cycles.

deposited nanostructured MoS₂@Ni-F and ZnS-MoS₂@Ni-F electrodes are 1763, 1334, 747, 556, and 270 and 3565, 1896, 1106, 837, and 495 F/g at 0.5, 1, 3, 5, and 10 mV s⁻¹, respectively. It is obvious that the C_{cv} values of the nanostructured ZnS-MoS₂@Ni-F electrode are greater than those of the nanostructured MoS₂@Ni-F electrode due to large current generation, surface area, and porous microstructures. The higher C_{cv} values (Figure 5c) of the nanostructured ZnS-MoS₂@Ni-F electrode are responsible for their excellent S-Cs performance. The porous microstructures help provide numerous defect-rich active sites for maximum diffusion/storage of electrolytic ions during the kinetic process, resulting in an excellent ECP ability of nanostructured electrodes. The measured C_{cv} values of

nanostructured MoS₂@Ni-F and ZnS-MoS₂@Ni-F electrodes are significantly larger than their reported C_{cv} values.^{33,35,37,39,54,57-62} The calculated C_{cv} values of the deposited nanostructured ZnS-MoS₂@Ni-F electrodes are significantly greater than the literature C_{cv} values even after 10,000 cycles. Figure 5D demonstrates the variant C_{cv} values versus scan rates. It is observed that the C_{cv} values are reduced at a higher scan rate but are significantly higher than those of the nanostructured MoS₂@Ni-F electrode. The active surface area does not fully participate to store electrolyte ions, resulting in lower C_{cv} values at higher scan rates. The reason behind the decreasing C_{cv} values with increasing scan rates is that the electrolytic ion cannot diffuse inside the deposited electrode surface due to inadequate time at a higher scan rate.

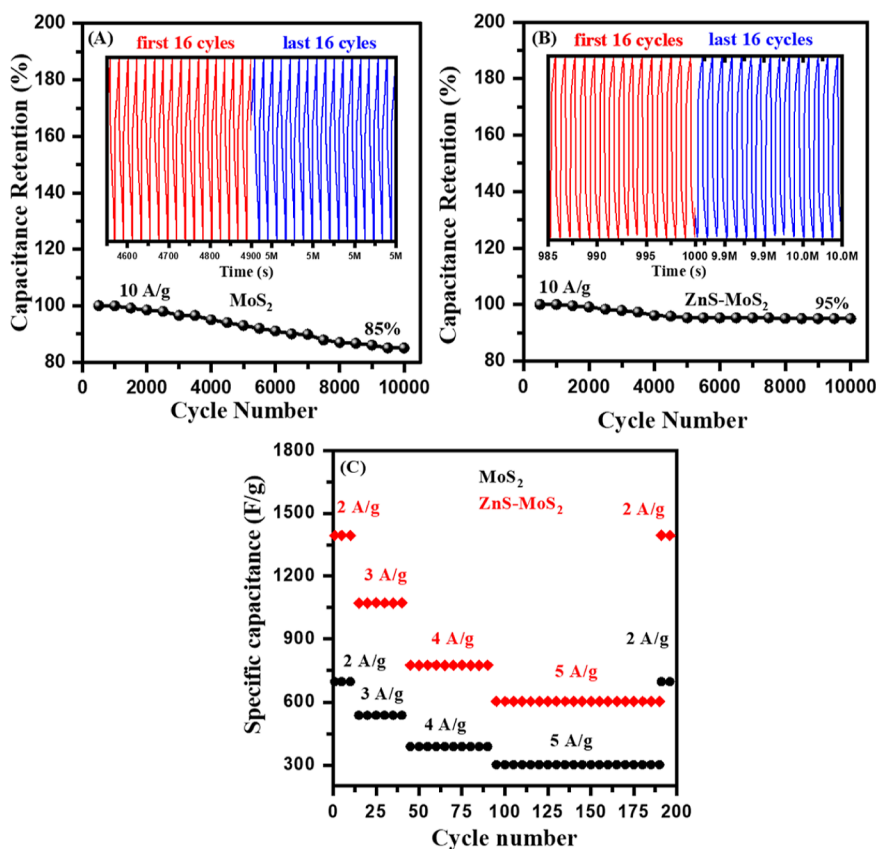


Figure 8. Variation in CR values of the nanostructured MoS₂@Ni-F (A) and ZnS–MoS₂@Ni-F (B) electrodes after 10,000 cycles at 10 A/g and cyclic reversibility (C) of the deposited electrodes.

Moreover, the C_{cv} values are also decreased due to large simulations of electrolytic ions leading to the phenomenon of concentration polarization.³⁸ The higher C_{cv} values of the nanostructured ZnS–MoS₂@Ni–F electrodes are due to the negligible concentration polarization, resulting in excellent rate capability.

The GCD measurements are studied to investigate the S–Cs behavior of the deposited nanostructured MoS₂@Ni–F and ZnS–MoS₂@Ni–F electrodes in voltage ranging from 0.25 to 0.42 V. The GCD profiles of the deposited nanostructured MoS₂@Ni–F and ZnS–MoS₂@Ni–F electrodes are studied at 1, 2, 3, and 5 A/g to observe the C_{cd} , CR, CS, and cycle reversibility.

The GCD profiles of the nanostructured MoS₂@Ni–F (A) and ZnS–MoS₂@Ni–F electrodes at 1, 2, 3, and 5 A/g (Figure 6A,B). The shapes of GCD profiles are symmetric in nature, indicating the excellent rate capability and reversibility of the deposited electrodes. The discharge time of the ZnS–MoS₂@Ni–F electrode is 3 times higher than that of the MoS₂@Ni–F electrode (Figure 6C), which is good for an excellent S–Cs ability. The C_{cd} values of the deposited nanostructured MoS₂@Ni–F and ZnS–MoS₂@Ni–F electrodes are estimated by the equation.^{49,56}

$$C_{cd} = \frac{J \times \Delta t}{\Delta V} \quad (6)$$

where Δt is discharging time (s) and ΔV is the potential range (V). The C_{cd} values of nanostructured MoS₂@Ni–F and ZnS–MoS₂@Ni–F electrodes are found to be 1451, 1003, 762, and 450 F/g and 3032, 2468, 1081, and 624 F/g at 1, 2, 3, and 5

A/g, respectively (Figure 7D). From the CV and GCD analysis, it is concluded that the nanostructured ZnS–MoS₂@Ni–F electrode is more appropriate due to an excellent ECP and thus can be used in PES devices. The S–Cs ability of the deposited electrodes is strongly associated with electronic conductivity,^{63,64} which is associated with the charge transfer resistance (R_{ct}). The EIS measurement (0.1 Hz–100 kHz) provides an idea about the overall electronic conductivity of the deposited nanostructured MoS₂@Ni–F and ZnS–MoS₂@Ni–F electrodes. The EIS analysis (0.1 Hz–100 kHz) is studied to determine the equivalent series resistance (ESR), R_{ct} and diffusion resistance (W_o) of the nanostructured MoS₂@Ni–F and ZnS–MoS₂@Ni–F electrodes. The EIS profiles of the nanostructured MoS₂@Ni–F and ZnS–MoS₂@Ni–F electrodes before and after 10,000 cycles are shown in Figure 7A,B, respectively. It is observed that the EIS profile is comprised of the appearance of a semicircle and linear part in the high/low frequency regions.⁶⁵ The ESR is the combined resistance of the substrate and active materials, which can be evaluated through the x -axis intercept, while the diameter of the semicircle is attributed to R_{ct} values⁶⁶ and slope of the EIS profile, which represents the diffusion rate of electrolyte ions in the deposited electrodes. The high slope values of the EIS profile are good for improving the electronic conductivity, fast diffusion of ions, and hence excellent ECP of the deposited electrodes.⁶⁷ It means that if the vertical line of the EIS graph is more along the y -axis (imaginary axis), the above-mentioned parameters are higher.

Moreover, these important parameters of EIS analysis strongly determine the overall kinetic behavior of the electrochemical process. The values of ESR for the deposited

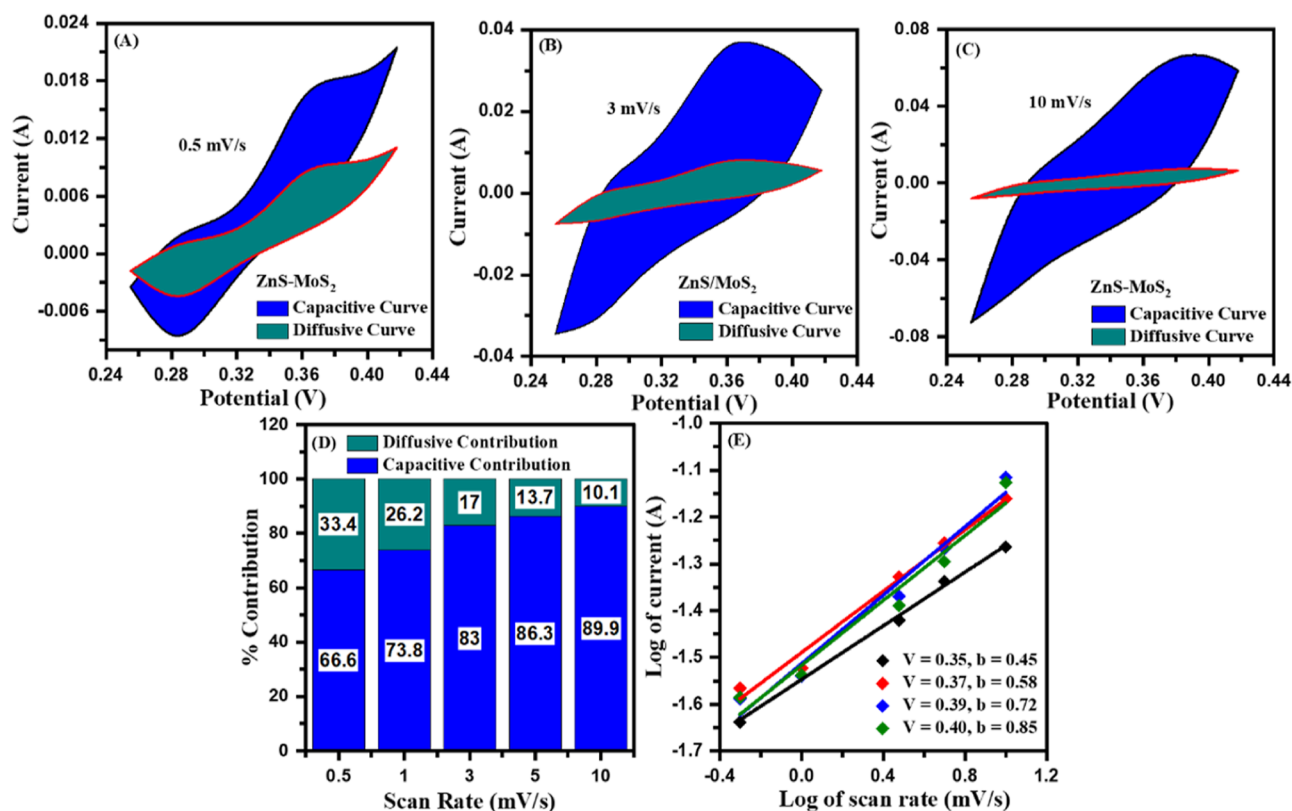


Figure 9. Capacitive-controlled and diffusive-controlled profiles of nanostructured ZnS-MoS₂@Ni-F electrodes at 0.5 mV/s (A), 3 mV/s (B), and 10 mV/s (C), the combined-percentage contributions at 0.5, 1, 3, 5, and 10 mV s⁻¹ (D), and the calculated *b*-values (E) of the nanostructured ZnS-MoS₂@Ni-F electrode.

nanostructured MoS₂@Ni-F and ZnS-MoS₂@Ni-F electrodes before/after 10,000 cycles are 2.79, 1.8, and 2.90, and 1.9 Ω, respectively. The minimum values of these resistances met by the ions in the kinetic process are responsible for favorable faradic redox reactions in the nanostructured MoS₂@Ni-F and ZnS-MoS₂@Ni-F electrodes. Moreover, no semicircle in EIS graphs of the deposited electrodes thereby confirms that the deposited electrode shows an excellent ECP (see inset zoom image). The absence of a semicircle is attributed to the excellent electrical conductivity, resulting in high charge storage capability of the deposited electrodes, which in turn results in good ECP for PES devices. The EIS profile of the nanostructured ZnS-MoS₂@Ni-F electrode is remarkably vertical as compared to the nanostructured MoS₂@Ni-F electrode, which represents the maximum electrolyte ion intercalation even after 10,000 cycles. The vertical straight line of the EIS graph is close to the 90° angle, which shows the ideal capacitive behavior of the deposited nanostructured ZnS-MoS₂@Ni-F electrode. It appears that the fast kinetics of the electrolytic ions is responsible for excellent ECP of the deposited electrodes. The maximum intercalation of ions is due to larger pore size distribution of the nanostructured ZnS-MoS₂@Ni-F electrode. The excellent diffusion and kinetic rates of the electrolytic ions are due to the creation of defect-rich microstructures comprising N-Ps-Rs-Ss (FESEM analysis). The CR and CS values from the GCD analysis are the key parameters to determine the long-term stability of the deposited electrodes for practical applications, especially in Li-ion-Bs and S-Cs for PES devices. The performance of the deposited electrodes remains unchanged even after 10,000 cycles at 10 A/g.

Figure 8A,B demonstrates the higher CR values (85 and 95%) of the nanostructured MoS₂@Ni-F and ZnS-MoS₂@Ni-F electrodes, respectively. The inset graphs show the CS behavior up to 10,000 C. The slight lowering in CR (15 and 5%) for the nanostructured MoS₂@Ni-F and ZnS-MoS₂@Ni-F electrodes might be due to changes in surface morphology like porosity, shape, and size of nanoparticles during the electrochemical process. The reduction in CR values is due to the creation of microstrains, stresses, and defects, followed by the change in surface morphology. These changes in physical properties may also be generated due to the rapid kinetic process of the electrolyte ions in working electrodes. Based on the above-mentioned results, the higher CR (%) value of the nanostructured ZnS-MoS₂@Ni-F electrode shows that it is more appropriate for the PES devices. Figure 8C exhibits the change in *C_{cd}* values of the nanostructured MoS₂@Ni-F and ZnS-MoS₂@Ni-F electrodes at 2, 3, 4, and 5 A/g for different numbers of cycles. It is observed that the *C_{cd}* values are nearly constant for different cycles at constant current densities. However, the *C_{cd}* values of the ZnS-MoS₂@Ni-F electrode are higher than those of the MoS₂@Ni-F electrode at all current densities. The *C_{cd}* values for both the deposited electrodes become low with the increasing values of current density; however, these values approach initial values when the GCD analysis is performed at lower current densities. This indicates that the deposited electrodes exhibit an excellent cyclic reversibility, which again makes it appropriate for the PES devices.

After the analysis of experimental results, the theoretical simulations are done to study the electrochemical parameters like capacitive- and diffusive-controlled contributions for the

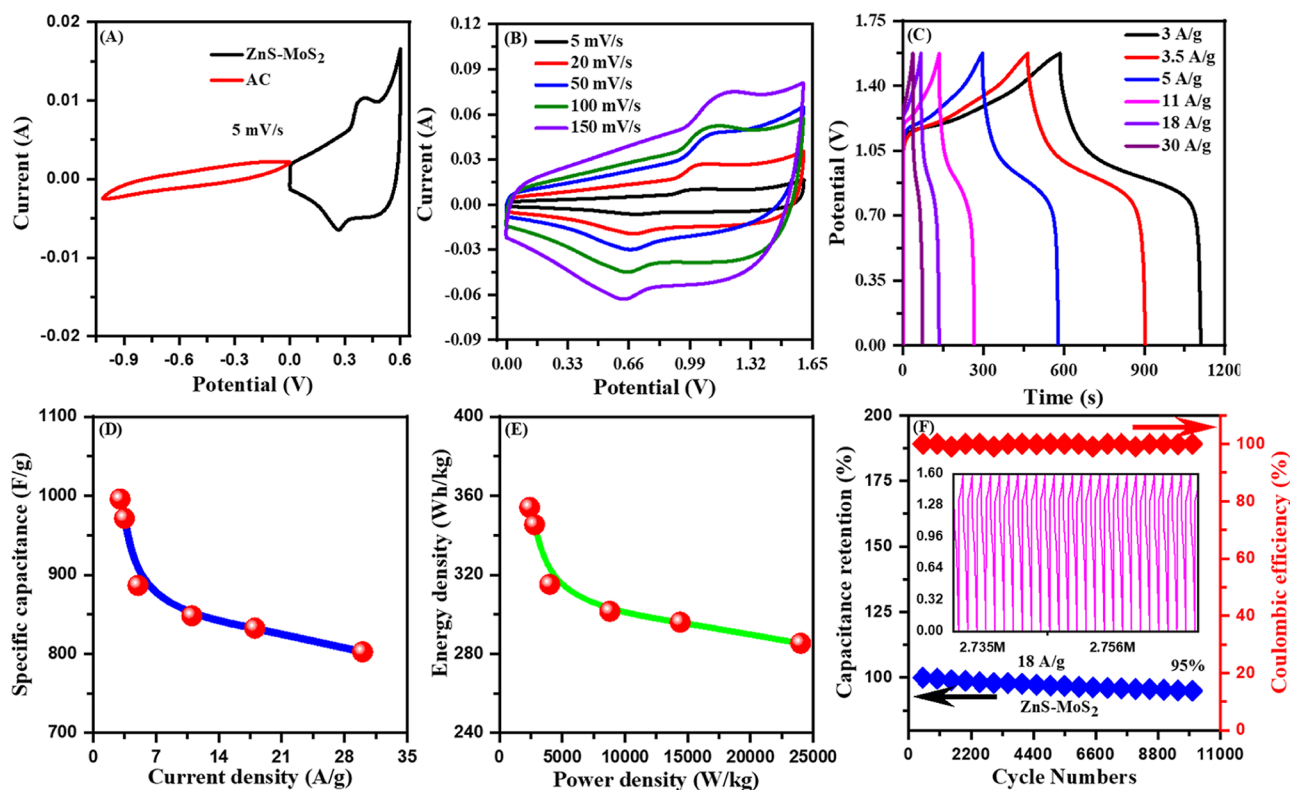


Figure 10. ECP of the asymmetric S–Cs device: CV profile of the AC and ZnS–MoS₂@Ni–F electrode at 5 mV/s (A), the combined CV profiles at 5, 20, 50, 100, and 150 mV/s (B), the combined GCD profiles at 3, 3.5, 5, 11, 18, and 30 A/g (C), the calculated C_{cd} values of asymmetric S–Cs (D), E_d vs P_d (E), and CR and CE (F) after 10,000 cycles.

overall S–Cs performance of the deposited nanostructured ZnS–MoS₂@Ni–F electrode. The capacitive and diffusive contributions are determined by the following equation^{68,69}

$$\frac{i(V)}{v^{1/2}} = k_1 v^{1/2} + k_2 \quad (7)$$

where i , k_1 , and k_2 represent the anodic/cathodic current in CV analysis at a specific value of potential (V), slope, and intercept by drawing the plot between $\frac{i(V)}{v^{1/2}}$ vs $v^{1/2}$ parameters, respectively. The theoretically calculated capacitive and diffusive profiles at 0.5, 3, and 10 mV/s are presented in Figure 9A–C, respectively. The value of the capacitive nature of the deposited electrodes is about 66%, which is about 2 times that of the diffusive nature at 0.5 mV/s. The values of the capacitive nature of the deposited electrode are increased up to 90%, whereas the values of diffusive nature are decreased up to 10%. This increasing capacitive nature of the deposited electrodes validates the author's previous claim that the diffusion of electrolytic ions is reduced at the maximum scan rate, which may be due to the inadequate time to diffuse the electrolytic ions into the surface of the deposited electrodes through intercalation and deintercalation processes. Figure 9D demonstrates the decreasing trend of the diffusive nature of electrolytic ions on the surface of the deposited electrodes. Based on the above-mentioned results, the capacitive contribution of the deposited electrodes is dominated at lower and higher scan rates. In short, the nanostructured ZnS–MoS₂@Ni–F electrode exhibits an excellent energy storage ability, enabling it to be a more interesting candidate for PES devices. To further clarify the aforementioned experimental results, theoretical power law simulations are performed to

investigate the nature of nanostructured ZnS–MoS₂@Ni–F electrodes. The P–Cs nature of the deposited nanostructured ZnS–MoS₂@Ni–F electrodes is calculated by the equation⁶⁹

$$i = av^b \quad (8)$$

where i is the anodic peak current and a and b are the constants.

The value of the constant b -parameter can be evaluated by the linearly fitted plot of log of anodic peak current versus log of the scan rate. If b is 1, the deposited electrodes have battery-type behavior, whereas if b is greater than 0.5 but less than 1, then it has hybrid behavior (combined battery and P–Cs). In the present case, the observed b -values are found to be 0.45, 0.58, 0.72, and 0.85 (Figure 9E), which suggest that the deposited nanostructured ZnS–MoS₂@Ni–F electrode has hybrid behavior.

3.4. Asymmetric S–Cs Performance. The deposited nanostructured ZnS–MoS₂@Ni–F electrode (exhibiting excellent energy storage ability) and activated carbon (AC) are employed as positive and negative electrodes for assembling asymmetric S–Cs devices, respectively. The +ve and –ve electrodes are isolated through filter paper to overcome the short-circuiting. Figure 10 shows the ECP of the asymmetric S–Cs device. Figure 10A exhibits the combined CV profile of AC and the nanostructured ZnS–MoS₂@Ni–F electrode at 5 mV/s. The nanostructured ZnS–MoS₂@Ni–F electrode presents the EDLCs and P–Cs nature, whereas the AC electrode only showed the EDLC behavior. The CV profiles of the asymmetric S–Cs device at 5, 20, 50, 100, and 150 mV/s are shown in Figure 10B. Again, the asymmetric S–Cs device shows the combined EDLCs and P–Cs behavior.

The presence of redox peaks even at 150 mV/s shows an excellent rate capability and the ECP of the asymmetric S–Cs device, which is due to high defect-rich microstructure active pores of the electrodes used in the assembling device. The small shifting in redox peaks indicates the minimum polarization effects that is attributed to the unique microstructural features of the ZnS–MoS₂@Ni–F electrode with the increasing scan rate. The GCD profiles (Figure 10C) are studied at 3, 3.5, 5, 11, 18, and 30 A/g to check the ECP of the asymmetric S–Cs device. The C_{cd} values of the asymmetric S–Cs device are found to be 996, 971, 886, 847, 832, and 802 F/g at all current densities. The E_d and P_d of asymmetric S–Cs device ranged from 354 to 285 W h/kg and 2400 to 24,000 W/kg (Figure 10E). The CR and CE of the asymmetric S–Cs device after 10,000 cycles are found to be 95 and 100% at 18 A/g, respectively. Results indicate that the assembled asymmetric S–Cs device exhibits an excellent S–Cs performance as compared to the reported asymmetric S–Cs devices.^{39,49,54,57–61}

4. CONCLUSIONS

Herein, the nanostructured hierarchical MoS₂@Ni–F and ZnS–MoS₂@Ni–F electrodes comprising N–Ps–Rs–Ss are deposited by a simple H–M CVD route. The XRD patterns confirm the formation of polycrystalline films growing along various orientations. The modification in structural and microstructural parameters shows the presence of lattice distortion, microstrains, stresses, and defect causes to enhance the ECP of S–Cs. The C_{cv} and C_{cd} values are found to be 1763 and 3565 F/g at 0.5 mV/s and 1451 and 3032 F/g at 1 A/g of the deposited electrodes, respectively. The growing behavior of impedance graphs indicates their capacitive nature; however, the shifting of impedance curves toward the y-axis indicates the increasing diffusion rates, which is because the development of nanostructured MoS₂@Ni–F and ZnS–MoS₂@Ni–F electrodes results in low impedance. The minimum capacity fading and larger electrical conductivity of the deposited electrodes are due to the combined effect of the EDLC and P–Cs nature, which is again confirmed by the theoretical simulation. The formation of rough and porous microstructure comprising N–Ps–Rs–Ss and randomly orientated nanosheets enhances the ECP of the deposited electrodes. The absence of charge transfer resistance and an excellent CR (95%) after 10,000 cycles shows that the deposited nanostructured ZnS–MoS₂@Ni–F electrodes are suitable for PES devices than the MoS₂@Ni–F electrode. The assembled asymmetric S–Cs device showed that the values of electrochemical parameters like C_{cd}, E_d, P_d, CR, and CE are found to be 996 F/g, 354 W h/kg, 24,000 W/kg, and 95 and 100% after 10,000 cycles, respectively. Results show that binder-free excellent electrode materials having high ECP can be deposited with a simple H–M–CVD route.

■ ASSOCIATED CONTENT

Data Availability Statement

The graphs mentioned in the manuscript are original; however, their original files will be available upon reasonable request from the corresponding author. Moreover, the research data of the manuscript can be made available online at the time of publication because if the research data made available online before the acceptance of manuscript, it may create problems like increase of similarities index and can also be used by the third party.

■ AUTHOR INFORMATION

Corresponding Author

Ijaz Ahmad Khan – PPEM-Lab, Department of Physics, Government College University Faisalabad, 38000 Faisalabad, Pakistan; orcid.org/0000-0002-3554-592X; Email: ijazahmad@gcuf.edu.pk

Authors

Asif Raza – PPEM-Lab, Department of Physics, Government College University Faisalabad, 38000 Faisalabad, Pakistan

Abdur Rasheed – PPEM-Lab, Department of Physics, Government College University Faisalabad, 38000 Faisalabad, Pakistan

Amjad Farid – PPEM-Lab, Department of Physics, Government College University Faisalabad, 38000 Faisalabad, Pakistan

Misbah Yousaf – PPEM-Lab, Department of Physics, Government College University Faisalabad, 38000 Faisalabad, Pakistan

Noman Ayub – PPEM-Lab, Department of Physics, Government College University Faisalabad, 38000 Faisalabad, Pakistan

Complete contact information is available at:

<https://pubs.acs.org/10.1021/acsomega.3c09560>

Notes

The authors declare no competing financial interest.

■ ACKNOWLEDGMENTS

The deposition of nanostructured hierarchical MoS₂@Ni–F and ZnS–MoS₂@Ni–F electrodes is accomplished at PPEM-Lab established under the LCF-10 project funded by HEC, Pakistan.

■ REFERENCES

- (1) Dahiya, Y.; Hariram, M.; Kumar, M.; Jain, A.; Sarkar, D. Modified transition metal chalcogenides for high performance supercapacitors: current trends and emerging opportunities. *Coord. Chem. Rev.* **2022**, *451*, 214265.
- (2) Shaikh, N. S.; Ubale, S. B.; Mane, V. J.; Shaikh, J. S.; Lokhande, V. C.; Praserthdam, S.; Lokhande, C. D.; Kanjanaboos, P. Novel electrodes for supercapacitor: conducting polymers, metal oxides, chalcogenides, carbides, nitrides, MXenes, and their composites with graphene. *J. Alloys Compd.* **2022**, *893*, 161998.
- (3) Wang, Y.; Zhang, L.; Hou, H.; Xu, W.; Duan, G.; He, S.; Liu, K.; Jiang, S. Recent progress in carbon-based materials for supercapacitor electrodes: a review. *J. Mater. Sci.* **2021**, *S6*, 173–200.
- (4) Liang, R.; Du, Y.; Xiao, P.; Cheng, J.; Yuan, S.; Chen, Y.; Yuan, J.; Chen, J. Transition metal oxide electrode materials for supercapacitors: a review of recent developments. *Nanomaterials* **2021**, *11* (5), 1248.
- (5) Choudhary, N.; Patel, M.; Ho, Y. H.; Dahotre, N. B.; Lee, W.; Hwang, J. Y.; Choi, W. Directly deposited MoS₂ thin film electrodes for high performance supercapacitors. *J. Mater. Chem. A* **2015**, *3*, 24049–24054.
- (6) Cherusseri, J.; Choudhary, N.; Sambath Kumar, K.; Jung, Y.; Thomas, J. Recent trends in transition metal dichalcogenide based supercapacitor electrodes. *Nanoscale Horiz.* **2019**, *4*, 840–858.
- (7) Li, R.; Wang, Y.; Zhou, C.; Wang, C.; Ba, X.; Li, Y.; Huang, X.; Liu, J. Carbon-stabilized high-capacity ferroferric oxide nanorod array for flexible solid-state alkaline battery–supercapacitor hybrid device with high environmental suitability. *Adv. Funct. Mater.* **2015**, *25*, 5384–5394.

- (8) Liu, L.; Niu, Z.; Chen, J. Unconventional supercapacitors from nanocarbon-based electrode materials to device configurations. *Chem. Soc. Rev.* **2016**, *45*, 4340–4363.
- (9) Agrawal, A.; Kumar, M.; Prajapati, D. K.; Singh, M.; Kumar, P. Smart public transit system using an energy storage system and its coordination with a distribution grid. *IEEE Trans. Intell. Transport. Syst.* **2014**, *15*, 1622–1632.
- (10) Nithya, V. D.; Arul, N. S. Review on α -Fe₂O₃ based negative electrode for high performance supercapacitors. *J. Power Sources* **2016**, *327*, 297–318.
- (11) Chen, W.; Shi, J.; Zhu, T.; Wang, Q.; Qiao, J.; Zhang, J. Preparation of nitrogen and sulfur dual-doped mesoporous carbon for supercapacitor electrodes with long cycle stability. *Electrochim. Acta* **2015**, *177*, 327–334.
- (12) Kalambate, P. K.; Dar, R. A.; Karna, S. P.; Srivastava, A. K. High performance supercapacitor based on graphene-silver nanoparticles-polypyrrole nanocomposite coated on glassy carbon electrode. *J. Power Sources* **2015**, *276*, 262–270.
- (13) Zhao, X.; Ran, F.; Shen, K.; Yang, Y.; Wu, J.; Niu, X.; Kong, L.; Kang, L.; Chen, S. Facile fabrication of ultrathin hybrid membrane for highly flexible supercapacitors via in-situ phase separation of polyethersulfone. *J. Power Sources* **2016**, *329*, 104–114.
- (14) Yang, K. S.; Kim, B. H. Highly conductive, porous RuO₂/activated carbon nanofiber composites containing graphene for electrochemical capacitor electrodes. *Electrochim. Acta* **2015**, *186*, 337–344.
- (15) Dai, H.; Zhao, Y.; Zhang, Z.; Yang, J.; Liu, S.; Zhou, J.; Sun, G. Ostwald ripening and sulfur escaping enabled chrysanthemum-like architectures composed of NiS₂/NiS@C heterostructured petals with enhanced charge storage capacity and rate capability. *J. Electroanal. Chem.* **2022**, *921*, 116671.
- (16) Zhou, R.; Wang, H.; Chang, J.; Yu, C.; Dai, H.; Chen, Q.; Zhou, J.; Yu, H.; Sun, G.; Huang, W. Ammonium intercalation induced expanded 1T-rich molybdenum diselenides for improved lithium ion storage. *ACS Appl. Mater. Interfaces* **2021**, *13*, 17459–17466.
- (17) Chen, Q.; Fu, Y.; Jin, J.; Zang, W.; Liu, X.; Zhang, X.; Huang, W.; Kou, Z.; Wang, J.; Zhou, L.; et al. In-situ surface self-reconstruction in ternary transition metal dichalcogenide nanorod arrays enables efficient electrocatalytic oxygen evolution. *J. Energy Chem.* **2021**, *55*, 10–16.
- (18) Yu, C.; Xu, H.; Sun, Y.; Zhao, X.; Hui, Z.; Gong, Y.; Chen, R.; Chen, Q.; Zhou, J.; Sun, G.; et al. The incorporation of expanded 1T-enriched MoS₂ boosts hybrid fiber improved charge storage capability. *Carbon* **2020**, *170*, 543–549.
- (19) Zhang, C. Y.; Sun, G. W.; Bai, Y. F.; Dai, Z.; Zhao, Y. R.; Gao, X. P.; Sun, G. Z.; Pan, X. B.; Pan, X. J.; Zhou, J. Y. Ultrastable lithium–sulfur batteries with outstanding rate capability boosted by NiAs-type vanadium sulfides. *J. Mater. Chem. A* **2020**, *8*, 18358–18366.
- (20) Sun, G.; Liu, J.; Zhang, X.; Wang, X.; Li, H.; Yu, Y.; Huang, W.; Zhang, H.; Chen, P. Fabrication of ultralong hybrid microfibers from nanosheets of reduced graphene oxide and transition-metal dichalcogenides and their application as supercapacitors. *Angew. Chem., Int. Ed.* **2014**, *53*, 12576–12580.
- (21) Ma, X.; Kolla, P.; Zhao, Y.; Smirnova, A. L.; Fong, H. Electrospun lignin-derived carbon nanofiber mats surface-decorated with MnO₂ nanowhiskers as binder-free supercapacitor electrodes with high performance. *J. Power Sources* **2016**, *325*, 541–548.
- (22) Zhao, B.; Huang, S. Y.; Wang, T.; Zhang, K.; Yuen, M. M.; Xu, J. B.; Fu, X. Z.; Sun, R.; Wong, C. P. Hollow SnO₂@Co₃O₄ core-shell spheres encapsulated in three-dimensional graphene foams for high performance supercapacitors and lithium-ion batteries. *J. Power Sources* **2015**, *298*, 83–91.
- (23) Zhou, X.; Chen, Q.; Wang, A.; Xu, J.; Wu, S.; Shen, J. Bamboo-like composites of V₂O₅/polyindole and activated carbon cloth as electrodes for all-solid-state flexible asymmetric supercapacitors. *ACS Appl. Mater. Interfaces* **2016**, *8*, 3776–3783.
- (24) Gopalakrishnan, K.; Sultan, S.; Govindaraj, A.; Rao, C. N. R. Supercapacitors based on composites of PANI with nanosheets of nitrogen-doped RGO, BC_{1.5}N, MoS₂ and WS₂. *Nano Energy* **2015**, *12*, 52–58.
- (25) Zhang, Y.; Ju, P.; Zhao, C.; Qian, X. In-situ grown of MoS₂/RGO/MoS₂@Mo nanocomposite and its supercapacitor performance. *Electrochim. Acta* **2016**, *219*, 693–700.
- (26) Wang, M.; Fei, H.; Zhang, P.; Yin, L. hierarchically layered MoS₂/Mn₃O₄ hybrid architectures for electrochemical supercapacitors with enhanced performance. *Electrochim. Acta* **2016**, *209*, 389–398.
- (27) Huang, Y.; Guo, J.; Kang, Y.; Ai, Y.; Li, C. M. Two dimensional atomically thin MoS₂ nanosheets and their sensing applications. *Nanoscale* **2015**, *7*, 19358–19376.
- (28) Lin, T.; Kang, B.; Jeon, M.; Huffman, C.; Jeon, J.; Lee, S.; Han, W.; Lee, J.; Lee, S.; Yeom, G.; et al. Controlled layer-by-layer etching of MoS₂. *ACS Appl. Mater. Interfaces* **2015**, *7*, 15892–15897.
- (29) Pumera, M.; Sofer, Z.; Ambrosi, A. Layered transition metal dichalcogenides for electrochemical energy generation and storage. *J. Mater. Chem. A* **2014**, *2*, 8981–8987.
- (30) Yang, R.; Fan, Y.; Zhang, Y.; Mei, L.; Zhu, R.; Qin, J.; Hu, J.; Chen, Z.; Hau Ng, Y.; Voiry, D.; et al. 2D transition metal dichalcogenides for photocatalysis. *Angew. Chem., Int. Ed.* **2023**, *62*, No. e202218016.
- (31) Zhang, D.; Sun, Y. E.; Li, P.; Zhang, Y. Facile fabrication of MoS₂-modified SnO₂ hybrid nanocomposite for ultrasensitive humidity sensing. *ACS Appl. Mater. Interfaces* **2016**, *8*, 14142–14149.
- (32) Stephenson, T.; Li, Z.; Olsen, B.; Mitlin, D. Lithium ion battery applications of molybdenum disulfide (MoS₂) nanocomposites. *Energy Environ. Sci.* **2014**, *7*, 209–231.
- (33) Shahbazi, M.; Khanlary, M. R. Study of optical, electrochemical, and morphological properties of MoS₂ thin films prepared by thermal evaporation. *Braz. J. Phys.* **2021**, *51*, 1182–1190.
- (34) Upadhyay, K. K.; Nguyen, T.; Silva, T. M.; Carmezim, M. J.; Montemor, M. F. Pseudocapacitive response of hydrothermally grown MoS₂ crumpled nanosheet on carbon fiber. *Mater. Chem. Phys.* **2018**, *216*, 413–420.
- (35) Manuraj, M.; Kavya Nair, K.; Unni, K. N.; Rakhi, R. B. High performance supercapacitors based on MoS₂ nanostructures with near commercial mass loading. *J. Alloys Compd.* **2020**, *819*, 152963.
- (36) Fu, L.; Xiong, W.; Liu, Q.; Wan, S.; Kang, C.; Li, G.; Chu, J.; Chen, Y.; Yuan, S. Metal-organic framework derived FeS/MoS₂ composite as a high performance anode for sodium-ion batteries. *J. Alloys Compd.* **2021**, *869*, 159348.
- (37) Luo, X.; Shao, J.; He, P.; Li, K.; Zhao, W. Construction of hierarchical ZnS/MoS₂ bimetallic sulfides heterostructures for high-performance sodium ion batteries. *Appl. Surf. Sci.* **2023**, *607*, 154821.
- (38) Saleem, S.; Salman, M.; Ali, S.; Ling, Y.; Khan, M. Electrocatalytic hydrogen evolution reaction on sulfur-deficient MoS₂ nanostructures. *Int. J. Hydrogen Energy* **2022**, *47*, 7713–7723.
- (39) Karade, S. S.; Dubal, D. P.; Sankapal, B. R. MoS₂ ultrathin nanoflakes for high performance supercapacitors: room temperature chemical bath deposition (CBD). *RSC Adv.* **2016**, *6*, 39159–39165.
- (40) Abdelaziz Aboelazm, E. A.; Mohammed Ali, G. A.; Algarni, H.; Chong, K. F. Flakes size-dependent optical and electrochemical properties of MoS₂. *Curr. Nanosci.* **2018**, *14*, 416–420.
- (41) Khan, I. A.; Rasheed, A.; Farid, A.; Yousaf, M.; Raza, A. Structural and optical properties of broccoli-based nanostructured ZnS films synthesized by powder vapor transport technique. *Opt. Quant. Electron.* **2023**, *55*, 133.
- (42) Khan, I. A.; Rasheed, A.; Farid, A.; Raza, A.; Yousaf, M.; Abbas, A. Structural, optical and dielectric properties of chemical vapor transport based synthesis of rice-like nanostructured cadmium zinc oxide films. *Thin Solid Films* **2023**, *768*, 139700.
- (43) Yousaf, M.; Rasheed, A.; Ahmad, M.; Farid, A.; Khan, I. A. Role of annealing temperature on structural and optical properties of zinc oxy-nitride films synthesized by powder vapor transport technique. *Ceram. Int.* **2022**, *48*, 15371–15379.

- (44) Raza, A.; Yousaf, M.; Rasheed, A.; Farid, A.; Khan, I. A. Synthesis of binder-free nanostructured MoS₂ films for optoelectronic applications. *Phys. B* **2023**, *670*, 415350.
- (45) Hussain, S. A.; Khan, I. A.; Ayub, M.; Rasheed, A. Study of structural, morphological and optical properties of ZnO and Mg-doped ZnO thin films synthesized by evaporation technique. *J. Ovonic Res.* **2021**, *17*, 571–580.
- (46) Mendoza-Sánchez, B.; Gogotsi, Y. Synthesis of two-dimensional materials for capacitive energy storage. *Adv. Mater.* **2016**, *28*, 6104–6135.
- (47) Bharathi, P.; Harish, S.; Mathankumar, G.; Krishna Mohan, M.; Archana, J.; Kamalakannan, S.; Prakash, M.; Shimomura, M.; Navaneethan, M. Solution processed edge activated Ni-MoS₂ nanosheets for highly sensitive room temperature NO₂ gas sensor applications. *Appl. Surf. Sci.* **2022**, *600*, 154086.
- (48) Liu, T.; Melinte, G.; Dolotko, O.; Knapp, M.; Mendoza-Sánchez, B. Activation of 2D MoS₂ electrodes induced by high-rate lithiation processes. *J. Energy Chem.* **2023**, *78*, 56–70.
- (49) Mishra, R. K.; Kushwaha, A. K.; Kim, S.; Seo, S. G.; Jin, S. H. Vertical-slate-like MoS₂ nanostructures on 3D-Ni-foam for binder-free, low-cost, and scalable solid-state symmetric supercapacitors. *Curr. Appl. Phys.* **2019**, *19*, 1–7.
- (50) Liu, H. Q.; Yao, C. B.; Li, J.; Sun, W. J.; Jiang, C. H. Modulating the electron transfer and resistivity of Ag plasma implanted and assisted MoS₂ nanosheets. *Appl. Surf. Sci.* **2022**, *571*, 151176.
- (51) Brafman, O.; Mitra, S. S. Raman effect in wurtzite-and zincblende-type ZnS single crystals. *Phys. Rev.* **1968**, *171*, 931–934.
- (52) Nilsen, W. G. Raman spectrum of cubic ZnS. *Phys. Rev.* **1969**, *182*, 838–850.
- (53) Cheng, Y. C.; Jin, C. Q.; Gao, F.; Wu, X. L.; Zhong, W.; Li, S. H.; Chu, P. K. Raman scattering study of zinc blende and wurtzite ZnS. *J. Appl. Phys.* **2009**, *106*, 123505.
- (54) Pujari, R. B.; Lokhande, A. C.; Shelke, A. R.; Kim, J. H.; Lokhande, C. D. Chemically deposited nano grain composed MoS₂ thin films for supercapacitor application. *J. Colloid Interface Sci.* **2017**, *496*, 1–7.
- (55) Patil, S.; Harle, A.; Sathaye, S.; Patil, K. Development of a novel method to grow mono-/few-layered MoS₂ films and MoS₂-graphene hybrid films for supercapacitor applications. *CrystEngComm* **2014**, *16*, 10845–10855.
- (56) Gong, H.; Zheng, F.; Li, Z.; Li, Y.; Hu, P.; Gong, Y.; Song, S.; Zhan, F.; Zhen, Q. Hydrothermal preparation of MoS₂ nanoflake arrays on Cu foil with enhanced supercapacitive property. *Electrochim. Acta* **2017**, *227*, 101–109.
- (57) Abraham, A. M.; Lonkar, S. P.; Pillai, V. V.; Alhassan, S. M. Three-dimensional MoS₂ nanodot-impregnated nickel foam electrodes for high-performance supercapacitor applications. *ACS Omega* **2020**, *5*, 11721–11729.
- (58) Ramadoss, A.; Kim, T.; Kim, G.-S.; Kim, S. J. Enhanced activity of a hydrothermally synthesized mesoporous MoS₂ nanostructure for high performance supercapacitor applications. *New J. Chem.* **2014**, *38*, 2379–2385.
- (59) Hu, R.; Huang, Z.; Wang, B.; Qiao, H.; Qi, X. Electrochemical exfoliation of molybdenum disulfide nanosheets for high-performance supercapacitors. *J. Mater. Sci.: Mater. Electron.* **2021**, *32*, 7237–7248.
- (60) Naz, R.; Abbas, W.; Liu, Q.; Shafi, S.; Gull, S.; Khan, S.; Rasheed, T.; Song, G.; Gu, J. Covalent functionalization of electrochemically exfoliated 1T-MoS₂ nanosheets for high-performance supercapacitor electrode. *J. Alloys Compd.* **2023**, *951*, 169944.
- (61) Sahoo, D.; Shakya, J.; Choudhury, S.; Roy, S. S.; Devi, L.; Singh, B.; Ghosh, S.; Kaviraj, B. High-performance MnO₂ nanowire/MoS₂ nanosheet composite for a symmetrical solid-state supercapacitor. *ACS Omega* **2022**, *7*, 16895–16905.
- (62) Wang, Z.; Wang, J.; Wang, F.; Zhang, X.; He, X.; Liu, S.; Zhang, Z.; Zhang, Z.; Wang, X. One-step hydrothermal synthesis of high-performance stable Ni-doped 1T-MoS₂ electrodes for supercapacitors. *J. Alloys Compd.* **2023**, *947*, 169505.
- (63) Neetika; Sanger, A.; Malik, V. K.; Chandra, R. One step sputtered grown MoS₂ nanoworms binder free electrodes for high performance supercapacitor application. *Int. J. Hydrogen Energy* **2018**, *43*, 11141–11149.
- (64) Yang, X.; Zhao, L.; Lian, J. Arrays of hierarchical nickel sulfides/MoS₂ nanosheets supported on carbon nanotubes backbone as advanced anode materials for asymmetric supercapacitor. *J. Power Sources* **2017**, *343*, 373–382.
- (65) He, Q.; Jiang, J.; Zhu, J.; Pan, Z.; Li, C.; Yu, M.; Key, J.; Shen, P. K. A facile and cost effective synthesis of nitrogen and fluorine Co-doped porous carbon for high performance sodium ion battery anode material. *J. Power Sources* **2020**, *448*, 227568.
- (66) Wang, H.; Tian, L.; Ali, M.; Zhao, X.; Han, S.; Xing, Z. Two-step electrodeposition synthesis of NiCo₂S₄/MoS_x composite on nickel foam as electrodes for supercapacitors. *J. Alloys Compd.* **2023**, *932*, 167628.
- (67) Iqbal, M. Z.; Khan, J. Optimization of cobalt-manganese binary sulfide for high performance supercapattery devices. *Electrochim. Acta* **2021**, *368*, 137529.
- (68) Simon, P.; Gogotsi, Y.; Dunn, B. Where do batteries end and supercapacitors begin? *Science* **2014**, *343*, 1210–1211.
- (69) Chao, D.; Zhu, C.; Yang, P.; Xia, X.; Liu, J.; Wang, J.; Fan, X.; Savilov, S. V.; Lin, J.; Fan, H. J.; et al. Array of nanosheets render ultrafast and high-capacity Na-ion storage by tunable pseudocapacitance. *Nat. Commun.* **2016**, *7*, 12122.